MNRAS **000**, 1–5 (2026) Preprint 27 July 2026 Compiled using MNRAS LATEX style file v3.3

Emissivity line ratios for [Mn III] and spectral diagnostics of H II regions

Zher Samak,[1] Sultana N. Nahar,[2] Anil K. Pradhan[2,3]
[1]*Al Aqsa University, Gaza, Palestine*
[2]*Department of Astronomy, The Ohio State University, Columbus, Ohio, USA 43210*
[3]*Chemical Physics Program, The Ohio State University, Columbus, Ohio, USA 43210*

Accepted XXX. Received YYY; in original form ZZZ

ABSTRACT

We present the first theoretical emission-line study of [Mn III] as potential determinant of physical conditions and manganese abundance. We compute atomic data for a set of [Mn III] lines and line emissivity ratios as temperature-density diagnostics. Accurate relativistic Breit-Pauli R-matrix calculations have been carried out for electron impact excitation of [Mn III] transitions that have not been previously studied. Selected forbidden lines are shown to be sensitive to temperature and density under nebular conditions in H II regions such as SNRs. The coupled channel R-matrix calculations include a wavefunction expansion that includes 38 levels of Mn III dominated by the ground and first excited electronic configurations $3d^5$ and $3d^44s$. Collision strengths for all 703 forbidden transitions among those levels, and Maxwellian averaged rate coefficients are obtained. A collisional-radiative model yields emissivity line ratios using calculated collision strengths and radiative decay A-values. Based on the present analysis, certain [Mn III] lines are predicted to be sensitive to density and/or in the typical nebular range. The detection of those lines could also yield cosmic Mn abundance relative to other elements.

Key words: atomic data – atomic processes – forbidden lines – electron impact excitation – ISM: abundances – ISM: supernova remnants – H II regions

Formation of Fe-group elements occurs via explosive supernovae nucleosynthesis (*e.g.* Nissen, P. E. et al. 2024; Ting & Weinberg 2022). Of these elements, Fe and Mn can both be produced in core collapse supernovae (SNe) Type II with massive stars as progenitors at the end of stellar nucleosynthesis, and in SNe Type Ia following a binary system explosion with white dwarf progenitors formed from low-mass stars. However, the timescales are quite different since massive stars have lifetimes of Myrs whereas white dwarf formation takes place at typical low-mass stellar lifetimes of Gyrs (Jomaron et al. 1999; Berg et al. 2015). Manganese is an odd-Z element and has a different temporal history than Fe. The Mn/Fe ratio increases with time or with Fe/H as function of the dichotomy between massive core collapse Supernovae Type II (SNe II) and Supernovae Type Ia (SNe Ia). Produced more efficiently in the neutron-rich environment of SNe Ia more than SNe II, the Mn abundance relative to Fe continues to increase and is therefore a chronometer of galaxy evolution, nucleosynthesis, and star formation history of the Universe. Abundance determinations are made from spectral lines. Generally, neutral Mn I absorption lines are measured from stellar atmospheres relative to Fe I to infer the abundance ratio, such as in the Milky Way APOGEE survey (Majewski et al. 2017; Smith et al. 2021; Melo et al. 2024). Whereas absorption by neutral Mn I is widely employed as a probe of Mn abundance through stellar spectral analysis, Mn ions have not been studied in emission. However, highly ionized Mn ions are detected in X-ray observations of supernova remnants. It is therefore expected that low ionization stages might be present in late nebular phases of SNRs, emitting in the UV/O/IR, and corresponding emission lines may provide useful information on physical conditions and abundances.

To our knowledge, emission lines from ionized Mn have not been employed for astrophysical diagnostics of physical conditions and elemental abundances from H II regions such as supernova remnants (SNRs). The primary reasons are twofold: (i) Mn abundance is lower than Fe by about a factor of 100 and spectral lines are difficult to detect, and (ii) singly ionized Mn II lines are in the UV and not readily observed from ground-based surveys. However, red-shifted lines from high-z objects are now well within the range of the JWST/NIRSpec and should be eminently observable. In this work we focus on relatively low-lying energy levels of [Mn III] and NUV/O/NIR forbidden line transitions and emissivity ratios, that could also lead to determination of gas phase abundance of Mn relative to other elements.

1 THEORY AND COMPUTATIONS

The atomic processes that give rise to emission lines considered in this work are briefly described below, in addition to the calculations and data obtained.

1.1 Energy levels and radiative transitions

The energy levels and Einstein A-coefficients for the forbidden $E2$ and $M1$ transitions among the fine-structure levels of the ground-state manifold in [Mn III] were calculated using the SUPERSTRUCTURE (SS) code (Eissner et al. 1974). The configuration interaction (CI) calculations included spectroscopic levels of the ground configuration $3d^5$ and a few levels of $3d^4s$, together with n = 4,5 correlation configurations: $3d^4$ $(4s, 4p, 4d, 4f, 5s, 5p, 5d)$. A total of 1421 fine-structure levels were computed by SS, spanning an energy range from

Table 1. Fine-structure energy levels of [Mn III] from the ground configuration $3d^5$. Level indices follow the NIST ordering. Energies are given in Rydberg (Ry). SS denotes the present SUPERSTRUCTURE calculations; NIST values are from Kramida et al. (2023).

Index	Configuration	Term	J	E_{SS} (Ry)	E_{NIST} (Ry)
1	$3d^5$	^6S	5/2	0.0000000	0.0000000
2	$3d^5$	^4G	11/2	0.2482025	0.2444419
3	$3d^5$	^4G	9/2	0.2481890	0.2446852
4	$3d^5$	^4G	5/2	0.2480204	0.2447463
5	$3d^5$	^4G	7/2	0.2481159	0.2447654
6	$3d^5$	^4P	5/2	0.2829707	0.2657956
7	$3d^5$	^4P	3/2	0.2831493	0.2661565
8	$3d^5$	^4P	1/2	0.2833889	0.2664672
9	$3d^5$	^4D	7/2	0.3036693	0.2944058
10	$3d^5$	^4D	1/2	0.3037763	0.2949670
11	$3d^5$	^4D	5/2	0.3041189	0.2951020
12	$3d^5$	^4D	3/2	0.3040145	0.2951111
13	$3d^5$	^2I	11/2	0.3571703	0.3569830
14	$3d^5$	^2I	13/2	0.3573770	0.3570030
15	$3d^5$	^2D	5/2	0.3940965	0.3757890
16	$3d^5$	^2D	3/2	0.3959121	0.3788120
17	$3d^5$	^2F	7/2	0.4067494	0.3882590
18	$3d^5$	^2F	5/2	0.4060531	0.3928050
19	$3d^5$	^4F	9/2	0.4170512	0.3970678
20	$3d^5$	^4F	7/2	0.4171292	0.3973352

the ground state $^6S_{5/2}$ to approximately 2.2 Ry. Of these, the lowest 38 levels dominated by the $3d^5$ and $3d^44s$ were selected as target states for subsequent (e + ion) scattering R-matrix calculations (described below). The selected fine-structure levels of the are of even parity, and all transitions among these occur via electric-quadrupole ($E2$) or magnetic-dipole ($M1$) relativistic operators. The calculated energy levels were compared with the available experimental values in the NIST Atomic Spectra Database (Kramida et al. 2023) to assess the reliability of atomic structure calculations prior to proceeding with calculations of transition probabilities and collision strengths. A comparison of the calculated SUPERSTRUCTURE energies with experimental values in the NIST Atomic Spectra Database (Kramida et al. 2023) for the lowest 20 fine-structure levels (Table 1) shows a mean difference of about 3 per cent with respect to NIST, providing a benchmark for the expected accuracy of the present atomic structure calculations. General accuracy of R-matrix data is estimated to be approximately 10–15 per cent based on experimental benchmarking (e.g. Sigut & Pradhan 1995, for Mg II).
(see Table 1). The forbidden $E2, M1$ line strengths and A-values are calculated using the SS code. The A-values within the forbidden fine-structure transitions of the ground configuration complex are generally small, in the range 10^{-3} to 10^2 s^{-1}. Table 2 gives a representative sample of the computed A-values that are employed in the line emissivity calculations.

1.2 Collisional excitation

The collision strengths, Ω_{ij}, for the $E2$ and $M1$ transitions among the fine-structure levels of the ground-state manifold in [Mn III] were calculated using the Breit–Pauli R-matrix (BPRM) method, widely employed for accurate and large-scale atomic calculations (Burke 2011; Hummer et al. 1993; Pradhan & Nahar 2011). The close coupling R-matrix calculations include channel couplings among the 38 energy levels of [Mn III], and the energy range considered extended up to the highest threshold is at 2.2 Ry and above up to 5.0 Ry. The collision strengths generally exhibit extensive resonance structures, particularly in the vicinity of excitation thresholds, arising from autoionizing levels associated with higher levels included in the close coupling expansion. For astrophysical applications, the plasma electrons are assumed to follow a Maxwellian distribution at a given electron temperature T_e, and therefore we compute the Maxwellian averaged effective collision strengths (Pradhan & Nahar 2011),

$$\Upsilon_{ij}(T_e) = \int_0^\infty \Omega_{ij}(E) \exp\left(-\frac{E}{kT_e}\right) d\left(\frac{E}{kT_e}\right), \quad (1)$$

where $\Omega_{ij}(E)$ is the collision strength at incident electron energy E, and k is the Boltzmann constant. The effective collision strength, $\Upsilon_{ij}(T_e)$, varies more smoothly and gradually with temperature than the raw collision strength, since the averaging process smooths out the sharp resonance structure. In the present work, Υ_{ij} was calculated at the electron temperatures 2500, 5000, 10000, 20000, 30000 and 40000 K, in order to cover the typical thermal range of astrophysical plasma environments in H II regions where [Mn III] may be observed. The collisional excitation rate is related to the effective collision strength through the excitation rate coefficient

$$q_{ij}(T_e) = \frac{8.629 \times 10^{-6}}{g_i T_e^{1/2}} \Upsilon_{ij}(T_e) \qquad (\text{cm}^3\ \text{s}^{-1}), \quad (2)$$

where $g_i = 2J_i + 1$ is the statistical weight of the initial level i.

Table 2. Selected forbidden transitions among the lowest 20 fine-structure levels of [Mn III] ($3d^5$ configuration).

No.	Upper level		Lower level		A (s^{-1})	λ (Å)
	Term	J	Term	J		
1	^4G	5/2	^6S	5/2	2.581(−08)	3674.16
2	^4G	7/2	^6S	5/2	8.384(−10)	3672.75
3	^4G	9/2	^6S	5/2	4.447(−12)	3671.67
4	^4P	5/2	^6S	5/2	2.989(−01)	3220.36
5	^4P	5/2	^4G	5/2	2.797(−06)	26073.21
6	^4P	5/2	^4G	7/2	5.145(−07)	26144.68
7	^4P	5/2	^4G	9/2	4.186(−08)	26199.60
8	^4P	3/2	^6S	5/2	1.951(−01)	3218.33
9	^4P	3/2	^4G	5/2	3.703(−07)	25940.64
10	^4P	3/2	^4G	7/2	3.068(−08)	26011.38
11	^4P	1/2	^6S	5/2	3.247(−05)	3215.61
12	^4P	1/2	^4G	5/2	1.788(−08)	25764.91
13	^4D	7/2	^6S	5/2	5.270(−04)	3000.85
14	^4D	7/2	^4G	5/2	6.119(−06)	16375.30
15	^4D	7/2	^4G	7/2	5.466(−05)	16403.46
16	^4D	7/2	^4G	9/2	6.268(−05)	16425.07
17	^4D	7/2	^4G	11/2	2.619(−05)	16429.05
18	^4D	7/2	^4P	5/2	6.609(−03)	44025.64
19	^4D	7/2	^4P	3/2	1.682(−06)	44408.86
20	^4D	1/2	^6S	5/2	7.604(−05)	2999.80
21	^4D	1/2	^4G	5/2	3.499(−05)	16343.86
22	^4D	1/2	^4P	5/2	5.838(−07)	43799.09
23	^4D	1/2	^4P	3/2	5.947(−03)	44178.36
24	^4D	1/2	^4P	1/2	9.842(−03)	44697.55
25	^4D	3/2	^6S	5/2	3.601(−03)	2997.45
26	^4D	3/2	^4G	5/2	3.150(−05)	16274.34
27	^4D	3/2	^4G	7/2	2.044(−05)	16302.16
28	^4D	3/2	^4P	5/2	2.998(−03)	43303.43
29	^4D	3/2	^4P	3/2	6.436(−03)	43674.12
30	^4D	3/2	^4P	1/2	2.889(−04)	44181.46
31	^4D	5/2	^6S	5/2	6.818(−03)	2996.42
32	^4D	5/2	^4G	5/2	4.978(−05)	16244.05
33	^4D	5/2	^4G	7/2	1.659(−05)	16271.76
34	^4D	5/2	^4G	9/2	2.007(−05)	16293.02
35	^4D	5/2	^4P	5/2	3.653(−03)	43089.58

1.3 Collisional-Radiative Model

In order to derive the spectral line emissivity ratios as functions of electron temperature T_e and electron density N_e, a collisional-radiative (CR) model was constructed using the SPECTRA code (Hoy et al. 2023; Pradhan & Nahar 2011). This model is based on solving the statistical equilibrium equations for coupled level populations coupled via collisional and radiative processes. The theoretical line emissivity is the amount of energy per unit time per unit volume for a given transition $j \longrightarrow i$, expressed as

$$I([\mathrm{Mn\,III}];\lambda_{ji}) = \frac{h\nu_{ji}A_{ji}}{4\pi}\frac{N_j}{\sum_k N_k}\frac{n(\mathrm{Mn\,III})}{n(\mathrm{Mn})} \times \frac{n(\mathrm{Mn})}{n(\mathrm{H})}n(\mathrm{H}) \quad \mathrm{erg\,cm^{-3}\,s^{-1}}. \tag{3}$$

N_j refers to the population of the upper state. Summation over N_k refers to the total population of all levels included in the CR calculation. The ratio n(Mn III)/n(Mn) is the ionization fraction of Mn III relative to total manganese, and n(Mn)/n(H) is the manganese abundance relative to hydrogen deduced from Hα ,Hβ , etc. In order to obtain line emissivities from Eq. (3), one needs ionization fractions Mn III/Mn in the plasma source at the appropriate temperature and density, and are model dependent (Pradhan & Nahar 2011; Osterbrock & Ferland 2006; Dopita & Sutherland 2013).

2 RESULTS AND DISCUSSION

Atomic structure and collisional-radiative calculations are carried out for all levels and transitions described above. A brief sample of those results is presented and discussed below.

2.1 Collision Strengths

The collision strengths, Ω_{ij}, for four selected forbidden transitions of Mn III are presented in Fig. 1 as functions of incident electron energy E (Ry), and BPRM collision strengths are obtained for 703 transitions among 38 target levels over the energy range 0.0–5.0 Ry. All four transitions exhibit resonances in Rydberg series converging on to higher levels included in the close coupling expansion up to the highest level at 2.2 Ry, beyond which there is a relatively smooth background.

Figs. 1a,b show collision strengths for the transitions ${}^4D_{7/2} \longrightarrow {}^4P_{5/2}$ (λ = 4.403 μm) and ${}^4D_{5/2} \longrightarrow {}^6S_{5/2}$ (λ = 0.300 μm), respectively, which correspond to the density diagnostic line ratios in Fig. 2.

2.2 Effective Collision Strengths

The effective Maxwellian averaged collision strengths (Eq. 1), $\Upsilon_{ij}(T_e)$, were obtained over a range of electron temperatures characteristic of H II regions (T_e = 2500–40000 K), that are relatively smoothly varying with T$_e$. For most transitions, the $\Upsilon_{ij}(T_e)$ exhibit a monotonic variation with temperature, reflecting the enhanced contribution of higher-energy electrons to collisional excitation. However, for transitions dominated by near-threshold resonances, departures from monotonic behaviour may occur at lower temperatures. The excitation rate coefficients are computed as in Eq. (2) in the CR model to obtain level populations. Calculated values of $\Upsilon_{ij}(T_e)$ for selected transitions are listed in Table 3.

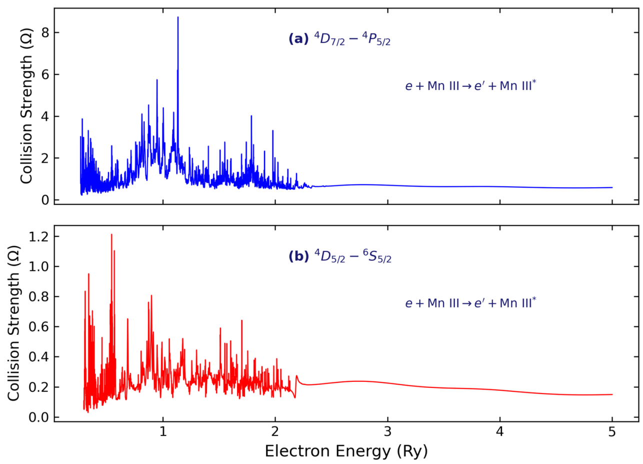

Figure 1. Collision strengths, Ω, for the forbidden transitions (a) ${}^4D_{7/2} \rightarrow {}^4P_{5/2}$ and (b) ${}^4D_{5/2} \rightarrow {}^6S_{5/2}$ in Mn III as functions of electron energy (Ry). Prominent resonance structures are present in the near-threshold region, while smoother behaviour is observed at higher energies.

2.3 Line Emissivity Ratios

When calculating the ratio between the intensities of two spectral lines as a function of electron density, two distinct behavioural regimes are identified depending on the energy separation of the levels involved and on the transition pair considered. For transitions between levels lying close to the ground state, characterized by small energy differences and relatively long wavelengths ($\lambda \sim$ 3–44 μm), the variation in the line ratio is noticeable over $3 \lesssim \log_{10} N_e \lesssim 7\,\mathrm{cm^{-3}}$. This behaviour arises because such levels are efficiently populated by electron-impact excitation even at relatively low electron densities. As the density increases beyond the critical density for these transitions, collisional de-excitation redistributes the level populations, causing the ratio to approach a density-independent value characteristic of local thermodynamic equilibrium (LTE) at high densities.

Fig. 2 presents four line emissivity ratios divided into two categories. The top row shows ratios nearly independent of electron temperature T_e, while the bottom row shows ratios sensitive to both N_e and T_e.

Panel (a) shows the ratio R_1, defined as the intensity of the ${}^4D_{5/2} \longrightarrow {}^6S_{5/2}$ transition at λ = 2996.42 Å to that of the ${}^4D_{3/2} \longrightarrow {}^6S_{5/2}$ transition at λ = 2997.45 Å. Both transitions originate from the ${}^4D$ multiplet and share the same lower level ${}^6S_{5/2}$, lying within a narrow ultraviolet interval, rendering this ratio insensitive to interstellar reddening and providing a clean density diagnostic over $3 \lesssim \log_{10} N_e \lesssim 7\,\mathrm{cm^{-3}}$, characteristic of planetary nebulae and H II regions.

Panel (b) shows R_2, the intensity of ${}^4D_{5/2} \longrightarrow {}^4P_{3/2}$ at 4.35 μm relative to ${}^4D_{3/2} \longrightarrow {}^4P_{5/2}$ at 4.33 μm, which lies in the mid-infrared and is accessible with JWST. Both R_1 and R_2 are virtually independent of T_e over the range 2500–40 000 K, confirming their utility as pure electron density diagnostics.

Panel (c) shows R_3, the ratio of ${}^4D_{7/2} \longrightarrow {}^4P_{5/2}$ at 4.40 μm to ${}^4D_{3/2} \longrightarrow {}^4P_{5/2}$ at 4.33 μm, which exhibits a strong dependence on T_e, particularly at low densities ($\log_{10} N_e \lesssim 4\,\mathrm{cm^{-3}}$), and is likewise observable with JWST.

Panel (d) presents R_4, the ratio of ${}^2F_{5/2} \longrightarrow {}^4P_{3/2}$ at 8213.52 Å to ${}^2D_{3/2} \longrightarrow {}^4P_{3/2}$ at 8081.28 Å, which increases monotonically with N_e and shows significant temperature sensitivity at all densities. The ratios R_3 and R_4 may be employed in combination with R_1 and R_2 to

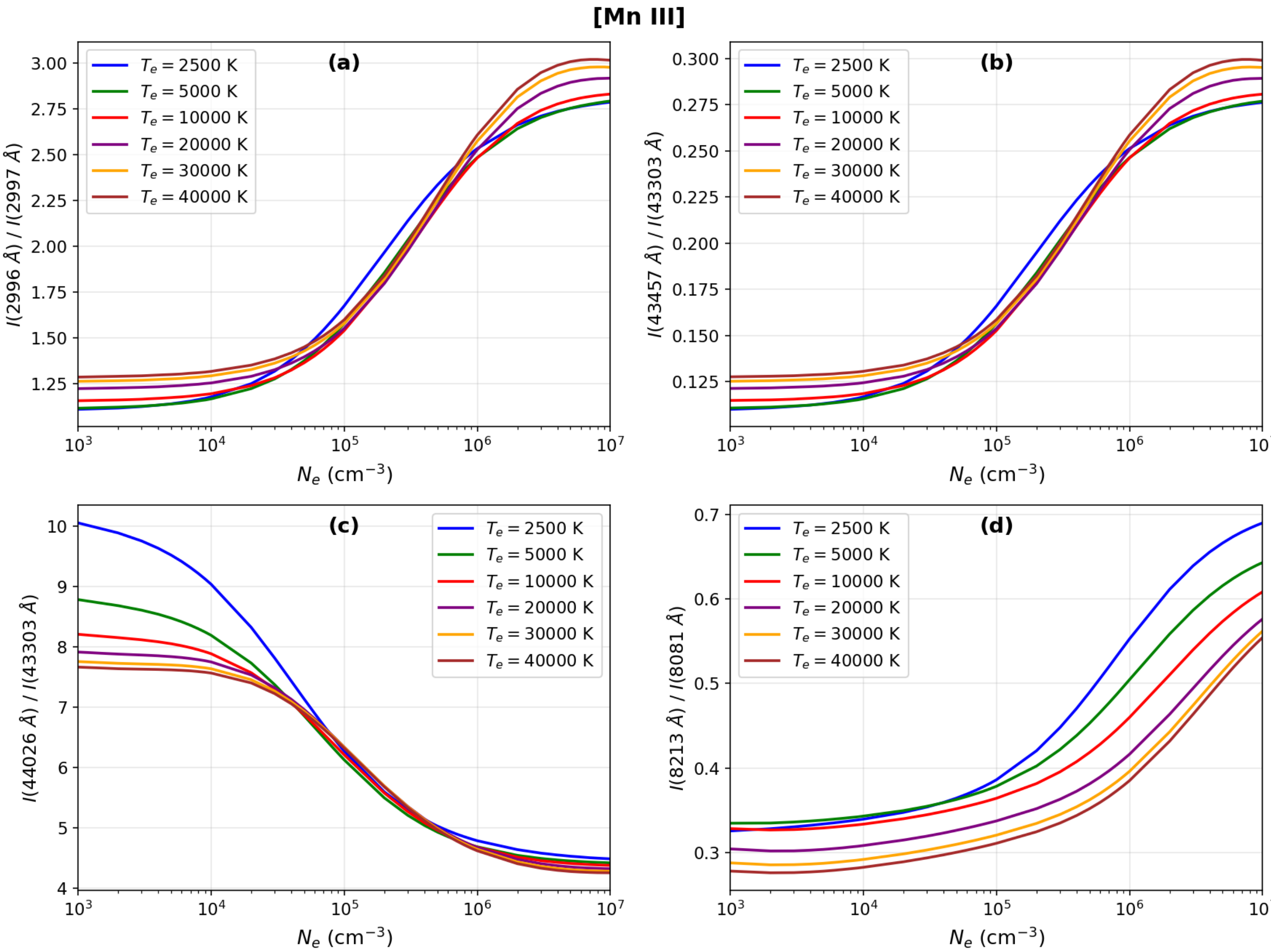

Figure 2. Mn III forbidden-line emissivity ratios as functions of $\log_{10}(N_e/\mathrm{cm}^{-3})$, at T_e = 2500, 5000, 10 000, 20 000, 30 000, and 40 000 K. Top row: ratios nearly independent of T_e: (a) R_1: $I(2996.42\,\text{Å})/I(2997.45\,\text{Å})$, ${}^4D_{5/2} \to {}^6S_{5/2}/{}^4D_{3/2} \to {}^6S_{5/2}$. (b) R_2: $I(4.35\,\mu\mathrm{m})/I(4.33\,\mu\mathrm{m})$, ${}^4D_{5/2} \to {}^4P_{3/2}/{}^4D_{3/2} \to {}^4P_{5/2}$. Bottom row: ratios sensitive to both N_e and T_e: (c) R_3: $I(4.40\,\mu\mathrm{m})/I(4.33\,\mu\mathrm{m})$, ${}^4D_{7/2} \to {}^4P_{5/2}/{}^4D_{3/2} \to {}^4P_{5/2}$. (d) R_4: $I(8213.52\,\text{Å})/I(8081.28\,\text{Å})$, ${}^2F_{5/2} \to {}^4P_{3/2}/{}^2D_{3/2} \to {}^4P_{3/2}$.

lift the degeneracy between electron temperature and density in H II regions. The resulting diagnostic line emissivity ratios are presented in Fig. 2 and divide into two distinct categories:

- **Pure electron density diagnostics (top row of Fig. 2):** The ultraviolet ratio R_1 (panel a), defined as $I(2996.42\,\text{Å})/I(2997.45\,\text{Å})$, involves two transitions within the ${}^4D$ multiplet sharing the common lower level ${}^6S_{5/2}$ at nearly identical wavelengths, and is therefore particularly robust against interstellar reddening and instrumental flux calibration uncertainties. The mid-infrared ratio R_2 (panel b), $I(4.35\,\mu\mathrm{m})/I(4.33\,\mu\mathrm{m})$, likewise falls within the observational reach of the James Webb Space Telescope (JWST). Both ratios are virtually insensitive to electron temperature across the full range T_e = 2500–40 000 K, and vary monotonically with electron density over $3 \lesssim \log_{10} N_e \lesssim 7\,\mathrm{cm}^{-3}$, making them reliable pure density diagnostics for planetary nebulae, H II regions, and SNRs.
- **Simultaneous temperature–density diagnostics (bottom row of Fig. 2):** The mid-infrared ratio R_3 (panel c), $I(4.40\,\mu\mathrm{m})/I(4.33\,\mu\mathrm{m})$, exhibits a strong dependence on T_e, particularly at low densities ($\log_{10} N_e \lesssim 4\,\mathrm{cm}^{-3}$), and is accessible with JWST. The near-infrared ratio R_4 (panel d), $I(8213.52\,\text{Å})/I(8081.28\,\text{Å})$, increases monotonically with N_e and shows significant temperature sensitivity at all densities. These two ratios may be employed in combination with R_1 and R_2 to break the degeneracy between electron temperature and density in nebular plasma diagnostics.

Following extensive analysis of emissivity ratios of all transitions considered in this work, we examine the tentative identification by Esteban et al. (2004, Table 2) Esteban et al. (2004) of a Mn III line at 6821.16 Å. However, with an uncertainty of, or exceeding, 40 per cent, this identification remains highly uncertain, and we cannot definitively confirm or rule out the presence of a spectral line at this wavelength. On the one hand, our calculations indicate that the two closest candidate transitions are ${}^4F_{7/2} \to {}^4P_{3/2}$ at 6801.52 Å and ${}^4F_{9/2} \to {}^4P_{5/2}$ at 6796.42 Å, which lie nearest in wavelength to the observed value. We computed the predicted intensity of each of these candidates relative to several strong, well-established reference lines within our spectral range, and found the candidate transitions to be markedly weak: their relative intensity ranged from approximately 26 to 45 times weaker than the R_4 diagnostic line (${}^2F_{5/2} \to {}^4P_{3/2}$, 8213.52 Å), and reached its most pronounced weakness – approximately 370 times weaker – when compared with a strong, nearby line (${}^2F_{7/2} \to {}^4G_{9/2}$, 5747.13 Å). Despite this consistent pattern of weakness observed across multiple independent comparisons, we cannot definitively rule out the presence of this line, since our calculations are limited to the relative strength of atomic transitions within the collisional-radiative model, and do not account for other factors that could substantially affect the actual observed intensity. Primary among these are the Mn III/Mn ionization fraction in the specific nebular environment under study (e.g. the Orion nebula) and the Mn/H abundance that are model dependent. It is possible, in principle, that the Mn III ion concentration is exceptionally low in the region observed, or that other physical factors beyond the scope of the present atomic model are involved, which could account for the observed weakness of the line without necessarily invalidating the proposed spectral identification.

3 CONCLUSIONS

We have presented the first systematic theoretical study of forbidden emission lines from doubly ionized manganese, [Mn III], aimed at establishing physical conditions and abundances in H II regions, supernova remnants (SNRs) and similar nebular environments. A comprehensive set of atomic data was computed for 1421 fine-structure energy levels of Mn III. Collision strengths Ω_{ij} for all 703 forbidden transitions among the lowest 38 fine-structure levels were computed using the Breit–Pauli R-matrix (BPRM) method (Hummer et al. 1993; Berrington et al. 1995). A CR model constructed using the SPECTRA code (Hoy et al. 2023; Pradhan & Nahar 2011) was employed to compute line emissivity ratios over the electron density range $3 \leq \log_{10} N_e \leq 7\,\mathrm{cm}^{-3}$. Complete datasets for Mn III will be described in a subsequent paper, and made available from the online database Nahar 2020a.

Employing the atomic data and line emissivities in this work, it should be possible to relate the manganese abundance to that of other elements and overall metallicity in H II regions. In particular, the Mn/Fe abundance ratio may be derived using JWST observations of high-z galaxies (*e.g.* (Nakane et al. 2025; Sarkar et al. 2025)). Atomic data and line ratios for Fe II have been obtained in previous works (Pradhan & Zhang 1993; Bautista et al. 1996), and may be employed for emission line analysis. In a recent work, we analyzed the temperature-abdundance dependent forbidden [O III] line ratios in high-z galaxies with data from JWST-VLT-Keck observations to infer the oxygen abundance and metallicity evolution with redshift, also using the canonical [O II] and [S II] forbidden lines as density diagnostics (Bhandari *et al.* 2026). Coupled with [Fe II] emission line diagnostics, the present work on [Mn III] may be employed to determine Mn/Fe ratios in a variety of sources as indicators of the chemical evolution of the Universe.

ACKNOWLEDGMENTS

This work was supported in part by the U.S. National Science Foundation grant AST-2407470. Partial computational work was carried out at the Ohio Supercomputer Center in Columbus, Ohio, USA.

DATA AVAILABILITY

The atomic data described herein will be made available from the online database NORAD (Nahar-OSU-Radiative-Atomic-Database; Nahar 2020b), or by correspondence with the authors.

Table 3. Effective Maxwellian-averaged collision strengths $\Upsilon_{ij}(T_e)$ for selected forbidden transitions of [Mn III] at T_e = 5000, 10 000, and 20 000 K. All levels belong to the $3d^5$ configuration.

Transition	λ (Å)	$\Upsilon(T_e)$		
		5000	10000	20000
$^6S_{5/2} - {}^4G_{11/2}$	3674.16	$8.582E-01$	$8.923E-01$	$9.770E-01$
$^6S_{5/2} - {}^4G_{9/2}$	3672.75	$8.202E-01$	$8.259E-01$	$8.680E-01$
$^6S_{5/2} - {}^4G_{5/2}$	3671.67	$7.029E-01$	$6.834E-01$	$7.056E-01$
$^4G_{11/2} - {}^4P_{5/2}$	26073.21	$6.476E-01$	$6.340E-01$	$6.115E-01$
$^4G_{5/2} - {}^4P_{5/2}$	26199.60	$4.938E-01$	$4.464E-01$	$3.952E-01$
$^6S_{5/2} - {}^4P_{3/2}$	3218.33	$3.696E-01$	$3.934E-01$	$3.934E-01$
$^6S_{5/2} - {}^4P_{1/2}$	3215.61	$1.819E-01$	$1.906E-01$	$1.889E-01$
$^6S_{5/2} - {}^4D_{7/2}$	3000.85	$7.084E-01$	$7.728E-01$	$7.992E-01$
$^6S_{5/2} - {}^4D_{5/2}$	2996.42	$2.136E-01$	$2.029E-01$	$1.977E-01$
$^6S_{5/2} - {}^4D_{3/2}$	2997.45	$4.459E-01$	$4.252E-01$	$4.104E-01$
$^4P_{3/2} - {}^4D_{5/2}$	43456.61	$1.667E-01$	$1.734E-01$	$1.804E-01$
$^4P_{5/2} - {}^4D_{3/2}$	43303.43	$3.300E-01$	$3.330E-01$	$3.338E-01$
$^4P_{3/2} - {}^4D_{3/2}$	43674.12	$2.758E-01$	$2.828E-01$	$2.974E-01$
$^4P_{5/2} - {}^4D_{7/2}$	44025.64	$8.761E-01$	$8.704E-01$	$8.744E-01$
$^4P_{3/2} - {}^4D_{3/2}$	43674.12	$2.758E-01$	$2.828E-01$	$2.974E-01$
$^4P_{5/2} - {}^4D_{7/2}$	44025.64	$8.761E-01$	$8.704E-01$	$8.744E-01$
$^4P_{5/2} - {}^4D_{3/2}$	43303.43	$3.300E-01$	$3.330E-01$	$3.338E-01$
$^4P_{3/2} - {}^2F_{5/2}$	8213.52	$3.670E-01$	$3.297E-01$	$3.070E-01$
$^4P_{3/2} - {}^2D_{3/2}$	8081.28	$2.946E-01$	$2.693E-01$	$2.613E-01$

REFERENCES

Bautista M. A., Peng J., Pradhan A. K., 1996, Astrophysical Journal v. 460, p. 372, 460, 372
Berg T. A. M., Ellison S. L., Prochaska J. X., Venn K. A., Dessauges-Zavadsky M., 2015, Monthly Notices of the Royal Astronomical Society, 452, 4326
Berrington K. A., Eissner W. B., Norrington P. H., 1995, Computer Physics Communications, 92, 290
Burke P. G., 2011, R-Matrix Theory of Atomic Collisions. Springer
Dopita M. A., Sutherland R. S., 2013, Astrophysics of the diffuse universe. Springer Science & Business Media
Eissner W., Jones M., Nussbaumer H., 1974, Computer Physics Communications, 8, 270
Esteban C., Peimbert M., García-Rojas J., Ruiz M. T., Peimbert A., Rodríguez M., 2004, MNRAS, 355, 229
Hoy K., Nahar S. N., Pradhan A. K., 2023, Monthly Notices of the Royal Astronomical Society: Letters, 521, L48–L52
Hummer D. G., Berrington K. A., Eissner W., Pradhan A. K., Saraph H. E., Tully J. A., 1993, Astronomy & Astrophysics, 279, 298
Jomaron C. M., Dworetsky M. M., Allen C. S., 1999, Monthly Notices of the Royal Astronomical Society, 303, 555
Kramida A., Ralchenko Y., Reader J., NIST ASD Team 2023, NIST Atomic Spectra Database (version 5.11), https://physics.nist.gov/asd
Majewski S. R., et al., 2017, The Astronomical Journal, 154, 94
Melo E., et al., 2024, The Astrophysical Journal, 973, 90
Nahar S. N., 2020a, Atoms, 8, 68
Nahar S., 2020b, Atoms, 8, 68
Nakane M., et al., 2025, The Astrophysical Journal, 994, 65
Nissen, P. E. Amarsi, A. M. Skúladóttir, Á. Schuster, W. J. 2024, A&A, 682, A116
Osterbrock D. E., Ferland G. J., 2006, Astrophysics of Gaseous Nebulae and Active Galactic Nuclei, 2nd edn. University Science Books, Sausalito
Pradhan A. K., Nahar S. N., 2011, Atomic astrophysics and spectroscopy. Cambridge University Press
Pradhan A. K., Zhang H. L., 1993, Astrophysical Journal, Part 2-Letters (ISSN 0004-637X), vol. 409, no. 2, p. L77-L79., 409, L77
Sarkar A., et al., 2025, The Astrophysical Journal, 978, 136
Sigut T. A. A., Pradhan A. K., 1995, Journal of Physics B: Atomic, Molecular and Optical Physics, 28, 4879
Smith V. V., et al., 2021, The Astronomical Journal, 161, 254
Ting Y.-S., Weinberg D. H., 2022, The Astrophysical Journal, 927, 209